




Test Particle Energization and the Anisotropic Effects of Dynamical MHD Turbulence

C. A. González¹, P. Dmitruk¹, P. D. Mininni¹, and W. H. Matthaeus² 

¹ Departamento de Física, Facultad de Ciencias Exactas y Naturales, Universidad de Buenos Aires and IFIBA, CONICET, Ciudad universitaria, 1428 Buenos Aires, Argentina; caangonzalez@df.uba.ar

² Bartol Research Institute and Department of Physics and Astronomy, University of Delaware, Newark, DE 19716, USA

Received 2017 April 8; revised 2017 September 6; accepted 2017 September 7; published 2017 November 13

Abstract

In this paper, we analyze the effect of dynamical three-dimensional magnetohydrodynamic (MHD) turbulence on test particle acceleration and compare how this evolving system affects particle energization by current sheet interaction, as opposed to frozen-in-time fields. To do this, we analyze the ensemble particle acceleration for static electromagnetic fields extracted from direct numerical simulations of the MHD equations, and compare it with the dynamical fields. We show that a reduction in particle acceleration in the dynamical model results from particle trapping in field lines, which forces the particles to be advected by the flow and suppresses long exposures to the strong electric field gradients that take place between structures and generate (among other effects) an efficient particle acceleration in the static case. In addition, we analyze the effect of anisotropy caused by the mean magnetic field. It is well known that for sufficiently strong external fields, the system experiences a transition toward a two-dimensional flow. This causes an increment in the size of the coherent structures, resulting in a magnetized state of the particles and a reduction in particle energization.

Key words: acceleration of particles – magnetohydrodynamics (MHD) – turbulence

1. Introduction

The production of energetic particles in the Earth–Sun environment and in the interstellar medium prompts a question: what are the mechanisms behind the generation of their nonthermally charged particle population (Parker & Tidman 1958)? In all of these systems the flows are turbulent, as the turbulent plasma state is observed in almost all astrophysical and space physics systems. Acceleration of charged particles by turbulence in the solar corona is also one of the candidates for explaining coronal heating, as well as the origin of solar wind energetic particles observed at in situ measurements and at ground-based observatories (McComas et al. 2007).

As a result, many authors have studied and reported charged particle acceleration by plasma turbulence (Matthaeus et al. 1984a; Lazarian et al. 2012). In general, turbulence covers a huge range of spatio-temporal scales, from low-frequency events well described by fluid plasma models (such as magnetohydrodynamics (MHD), and Hall-MHD) to very-high-frequency scales related to electron dynamics, which are well described by purely kinetic approaches.

In order to capture at least a fraction of the range of scales involved in plasma turbulence, test particle simulations in MHD flows have been used as a way to understand how the macroscopic behavior of a plasma could itself generate plasma heating and particle energization. This problem has been treated in different ways, which can be divided into two broad approaches. The first one consists of modeling the turbulence as a random collection of waves (Chandran 2003; Chandran & Maron 2004; Cho & Lazarian 2006; Lynn et al. 2013), a representation that cannot retain the coherent structures' formation and evolution, and which in particular can play a crucial role in particle energization (Matthaeus et al. 1984a; Tessein et al. 2015). In the second approach, the turbulence is generated as a result of the normal evolution of the MHD fluid equations (Dmitruk et al. 2004; Dmitruk & Matthaeus 2006a; Lehe et al. 2009; Dalena et al. 2014; Teaca et al. 2014; Weidl et al. 2015), and as such it self-consistently includes the

evolution of coherent structures. However, test particle studies have been mostly carried out using static fields obtained from the direct numerical simulation of the MHD equations (i.e., the system is evolved in time to reach a turbulent regime, and then a frozen-in-time snapshot of electric and magnetic fields is used to compute particle acceleration). The problem with this method is that it ignores the evolution of the coherent structures, and does not allow for the presence of waves.

Although there are some works that deal with the influence of dynamic MHD turbulence on test particles (Lehe et al. 2009; Teaca et al. 2014), those papers do not present a complete analysis of the dynamical field effects, which is in principle our main goal in this paper. Besides, the comparison between static and dynamic cases allows us to determine the most relevant mechanisms for particle heating, such as, e.g., particle-wave resonance or the interaction with well-developed coherent structures in the turbulent flow.

The first aim of this paper is to look at the effect of dynamical turbulence evolution on particle energization. To this end, we performed different direct numerical simulations of MHD turbulence, together with solving the equations for test particles with a gyroradius of the order of the MHD dissipation scale, first in static and then in dynamic electromagnetic fields, and for different values of a mean external magnetic field, B_0 . We found a reduction of particle energization in the dynamical case, and also that this reduction is the result of particle trapping by the dynamically evolving field lines. This trapping reduces the exposure time of the particles to regions of strong electric field gradients that take place at the interface between current sheets, and are an essential ingredient for efficient particle energization. In spite of this reduction, the results validate previously reported particle acceleration mechanisms in MHD turbulence (Matthaeus et al. 1984a; Dmitruk et al. 2004; Dalena et al. 2014; Teaca et al. 2014; Gonzalez et al. 2016) and show the importance of coherent structures in particle acceleration phenomena.

The second aim of this paper is to quantify the role of the mean external field, B_0 , in coherent structure formation and particle acceleration, as, in many cases in space physics, the particle acceleration takes place in the presence of a guide field. To do this, we performed a set of simulations varying the guide field from an isotropic case ($B_0 = 0$) up to a strong anisotropic case with a mean field $B_0 = 8$ (in units of the fluctuating magnetic field, \mathbf{b}). We show that the anisotropy induced by the mean magnetic field produces large coherent structures as the mean field increases. Consequently, for large magnetic field, the particles remain magnetized, that is, attached closely to magnetic field lines, and then cannot move across the current sheets, decreasing the possibility of them remaining in the aforementioned regions where the electric field gradients are strong. The particle propagation along the magnetic field lines then suppresses the acceleration due to perpendicular electric field gradients between current sheet structures.

Before proceeding we should remark on the relevance of this study, and others, on different particle species. For a given particle momentum and charge, the magnetic field strength controls the gyroradius, r_L . This scale must be compared to the length scales that characterize the turbulence, notably the outer or energy containing scale, λ_c , and the scale that terminates the inertial range, usually the Kolmogorov scale, λ_η , in magneto-fluids. Usually in plasmas we substitute for λ_η the larger of the ion inertial scale, d_i , and the thermal proton gyroradius, ρ_i , as the larger of these two scales characterizes the termination of the inertial range (“ $k^{-5/3}$ ”; Leamon et al. 1998; Chen et al. 2014). High-rigidity particles with $r_L/\lambda_c > 1$ are typically at very high energies and have characteristic and relatively simple transport properties (e.g., Bieber et al. 1994; Subedi et al. 2017). Particles with r_L lying in the inertial range $\lambda_c > r_L > d_i$ (or ρ_i) exhibit resonant scattering (Jokipii 1966; Bieber et al. 1994; Subedi et al. 2017) and therefore one generally finds that their magnetic moments (Dalena et al. 2014) are not well preserved in time. For the present purposes, these can be called “medium energy” particles.

Still lower rigidity particles with $r_L/d_i < 1$ or $r_L/\rho_i < 1$ do not experience strong resonant scattering, and may preserve their magnetic moments for longer times. Furthermore, plasma turbulences such as the solar wind, current sheets, vortex structures, and other coherent structures associated with dissipative scale intermittency are typically found with sizes of the order of d_i . Therefore, roughly speaking, smaller gyroradius particles (low rigidity) will not experience robust pitch angle scattering, and these same particles can remain “trapped” within current sheets or other small-scale coherent structures (Khabarova et al. 2016) for long enough periods of time that they may experience significant energization (Ambrosiano et al. 1988). Such particles include electrons, for many parameters of interest. Many studies (e.g., Matthaeus et al. 1984b; Dmitruk et al. 2004; Oka et al. 2010; Dahlin et al. 2014; Guo et al. 2014; Li et al. 2015) have provided theoretical insight concerning the diverse effects such as trapping, multiple magnetic islands, first- and second-order Fermi processes (Ambrosiano et al. 1988; Drake et al. 2005, 2006), etc., that may influence the energization of these low-rigidity, relatively low-energy particles.

For the medium energy particles, a different regime is realized because the pertinent physical effects change when the particle gyroradii of interest exceeds the typical inner scale, d_i or ρ_i , or a few times this scale. (Secondary magnetic islands and

flux ropes associated with reconnection, as well as the dominant current channels in turbulence, and the “break point” in the magnetic power spectrum, are often found to be a few times the inner scale.) Particles with these higher rigidities must have different properties because they can experience pitch angle scattering, and they sample somewhat larger scale electromagnetic structures. However, these particles cannot be easily trapped in current channels and small secondary magnetic structures that are the size of the inner scale of turbulence. Such particles typically include the suprathermal proton population (with speeds larger than the thermal or Alfvén speeds). Given the differences in these properties, it would not be surprising to find that the detailed mechanisms of energization differ for these medium energy protons. Indeed, there is little reason to expect that the mechanisms proposed above for lower-rigidity electrons will remain relevant for the larger gyroradii suprathermal protons. It is the further elucidation of the mechanisms that energize the latter class of protons that is the subject of the present paper.

The organization of this paper is as follows. In Section 2, we describe the model used in our investigations, the equations and properties of turbulent MHD fields, and the test particle model including the parameters that relate particles and fields. In Section 3.1, we present a comparison between the static and dynamic cases for an isotropic flow with $B_0 = 0$, and for an anisotropic flow with $B_0 = 2$. In Section 3.2, we discuss the effect of the mean magnetic field on coherent structures and particle acceleration. Finally, in Section 4, we discuss our findings and present our conclusions.

2. Models

The macroscopic description of the plasma adopted here is modeled by the following three-dimensional compressible MHD equations: the continuity (density) equation, the equation of motion, the magnetic field induction equation, and the equation of state. These are given, respectively, by Equations (1)–(4), which involve fluctuations of the velocity field \mathbf{u} , magnetic field \mathbf{B} , and density ρ . We assume a large-scale background magnetic field, B_0 , in the z -direction, so that the total magnetic field is $\mathbf{B} = \mathbf{B}_0 + \mathbf{b}$ with $\mathbf{B}_0 = B_0\hat{z}$,

$$\frac{\partial \rho}{\partial t} + \nabla \cdot (\mathbf{u}\rho) = 0, \quad (1)$$

$$\frac{d\mathbf{u}}{dt} = -\frac{\nabla p}{\rho} + \frac{\mathbf{J} \times \mathbf{B}}{4\pi\rho} + \nu \left(\nabla^2 \mathbf{u} + \frac{\nabla \nabla \cdot \mathbf{u}}{3} \right) + \mathbf{F}, \quad (2)$$

$$\frac{\partial \mathbf{B}}{\partial t} = \nabla \times (\mathbf{u} \times \mathbf{B}) + \eta \nabla^2 \mathbf{B} + \nabla \times \boldsymbol{\varepsilon}, \quad (3)$$

$$\frac{p}{\rho^\gamma} = \text{constant}. \quad (4)$$

In these equations, p is the pressure, ν is the viscosity, η is the magnetic diffusivity, $\mathbf{J} = \nabla \times \mathbf{B}$ is the current density, \mathbf{F} is an external mechanical force, and $\boldsymbol{\varepsilon}$ is an external electromotive force. We assume a polytropic equation of state $p/p_0 = (\rho/\rho_0)^\gamma$, with $\gamma = 5/3$, where p_0 and ρ_0 are, respectively, the equilibrium (reference) pressure, and density. The Hall current is not taken into account in Equation (3), but will be (nominally) included later on in the particle motion equations through the generalized Ohm’s law for the electric field. The reason for this is because the dynamics of the \mathbf{u} and \mathbf{B} fields described by Equations (1)–(4),

and of the particles we will consider, is not notably affected by the presence of the Hall term, provided that the Hall scale (see below) is close to the dissipation scale (see Dmitruk & Matthaeus 2006a, 2006b).

The magnetic and velocity fields here are expressed in Alfvén speed units based on field fluctuations. This Alfvén speed based on field fluctuations is defined as $v_0 = \sqrt{\langle b^2 \rangle / 4\pi\rho_0}$. A characteristic plasma velocity can also be given by the parallel Alfvén wave velocity along the mean magnetic field, $v_A = B_0 / \sqrt{4\pi\rho_0}$; this is proportional to the amplitude of the guide field. The ratio of fluid equilibrium pressure, p_0 , to magnetic pressure, B_0^2 , the so-called β of the plasma, is $\beta = p_0 / B_0^2 = 1 / (MB_0)^2$. The sonic Mach number $M = v_0 / C_s$ relates the mean velocity field with the sound speed $C_s = \sqrt{\gamma p_0 / \rho_0}$. We use the isotropic MHD turbulence correlation length, L , as a characteristic length (also called the energy containing scale), defined as $L = L_{\text{box}} \int (E(k)/k) dk / \int E(k) dk$, where $E(k)$ is the energy spectral density at wavenumber k , and L_{box} is the linear size of the domain. The unit timescale, t_0 , also called the eddy turnover time, is derived from the unit length and from the fluctuation in Alfvén speed $t_0 = L/v_0$.

The MHD equations are solved numerically using a Fourier pseudospectral method with periodic boundary conditions in a normalized cube of size $L_{\text{box}} = 2\pi$; this scheme ensures exact energy conservation for the continuous-time spatially discrete equations in the ideal ($\nu = \eta = 0$) and not forced ($\mathbf{F} = \boldsymbol{\varepsilon} = 0$) case (Mininni et al. 2011). The discrete time integration is done with a high-order Runge–Kutta method, and a resolution of 256^3 Fourier modes is used. For the kinematic Reynolds number $R = v_0 L / \nu$ and the magnetic Reynolds number $R_m = v_0 L / \eta$, we take $R = R_m = 1000$, which are limited here by the available spatial resolution. The Mach number in our simulations is $M = 0.25$, so we consider a weak compressible case.

In Gonzalez et al. (2016), we reported the effect of the compressibility of the flow on particle acceleration. In that study, we considered decaying turbulence from an initial perturbation, and after the turbulence was fully developed, the test particles were injected into the system and evolved in a frozen-in-time snapshot of the turbulent electromagnetic field. In this paper, we are interested in studying the effect of dynamically evolving turbulence; in order to maintain energy fluctuating around a mean value (i.e., to reach a turbulent steady state), we must force the system externally using the mechanical and electromotive forces, \mathbf{F} and $\boldsymbol{\varepsilon}$, in Equations (2) and (3). To this end, we started the system from initially null magnetic and velocity fields and forced it into a quasi-stationary turbulent MHD state. The forcing scheme that we employed (for both \mathbf{F} and $\boldsymbol{\varepsilon}$) in all of the simulations shown here is based on that presented in Pouquet & Patterson (1978). On average, the forcing introduces zero mechanical and magnetic helicity, and zero cross-correlation between velocity and magnetic field fluctuations. We used slowly evolving random-phase forcings in the Fourier k -shells with $3 \leq k \leq 4$, with a correlation time $\tau = t_0$. In other words, in each eddy turnover time new random (and uncorrelated) forcing functions \mathbf{F} and $\boldsymbol{\varepsilon}$ were generated, and each forcing was linearly interpolated in time from the previous random state to the new one in a time, t_0 . In this way, we prevented the introduction of sudden changes in the field that may arise when delta-correlated

in time forcing is used, and which may affect the evolution of test particles.

Each random snapshot of the forcing functions was generated as follows. For a forcing \mathbf{f} (which may be either \mathbf{F} or $\boldsymbol{\varepsilon}$), we generated the first two random fields in Fourier space,

$$\mathbf{v}_j^{(1)}(\mathbf{k}) = A(k)e^{i\phi_j}, \quad \mathbf{v}_j^{(2)}(\mathbf{k}) = A(k)e^{i\psi_j}, \quad (5)$$

where $j = 1, 2, 3$ are the field Cartesian components, $\phi_j(\mathbf{k})$ and $\psi_j(\mathbf{k})$ are random phases, and the amplitude is $A(k) = 1$ if $3 \leq k \leq 4$, and 0 otherwise. Two normalized incompressible fields are then constructed as

$$\mathbf{f}^{(1)} = \frac{\nabla \times \mathbf{v}^{(1)}}{\langle |\nabla \times \mathbf{v}^{(1)}|^2 \rangle^{1/2}}, \quad \mathbf{f}^{(2)} = \frac{\nabla \times \mathbf{v}^{(2)}}{\langle |\nabla \times \mathbf{v}^{(2)}|^2 \rangle^{1/2}}. \quad (6)$$

We introduce a correlation between these fields making use of an auxiliary quantity

$$\boldsymbol{\omega}_f = \nabla \times [\sin(\alpha)\mathbf{f}^{(1)} + \cos(\alpha)\mathbf{f}^{(2)}], \quad (7)$$

where α can take any value between 0 and $\pi/4$. Finally, the forcing function \mathbf{f} is given by

$$\mathbf{f}(\mathbf{k}) = f_0 \left[\cos(\alpha)\mathbf{f}^{(1)}(\mathbf{k}) + \sin(\alpha)\mathbf{f}^{(2)}(\mathbf{k}) + \frac{\boldsymbol{\omega}_f(\mathbf{k})}{k} \right], \quad (8)$$

with f_0 the forcing amplitude. Note that α controls how much correlated is \mathbf{f} with its curl (in fact, this correlation is proportional to $\sin 2\alpha$). Thus, using $\alpha = 0$ gives a random forcing function that does not inject helicity on the average. This allows us to study cases in which there is no inverse cascade (as the presence of helicity in the three-dimensional flow can result in the growth of large-scale structures as a result of the inverse cascade of magnetic helicity, see Mininni 2011), which will be important to understand the role of the growth of correlation lengths as the flow becomes two-dimensional in particle acceleration for large values of B_0 .

When a stationary turbulent state was reached and a broad range of scales were excited, the test particles were injected and then both fields and particles were simultaneously evolved (for frozen-in-time simulations, one snapshot of the fields was extracted, and only test particles were evolved). In the turbulent regime, the fluid contains energy from the outer scale L to the Kolmogorov dissipation scale $l_d = (\nu^3 / \epsilon_d)^{1/4}$, where ϵ_d is the average rate of energy dissipation; then we can define the Kolmogorov dissipation wavenumber as $k_d = 2\pi/l_d$.

We must now introduce the equations for the test particles, and associate the particle parameters with the relevant flow parameters. Test particle dynamics is described by the nonrelativistic equation of motion:

$$\frac{d\mathbf{v}}{dt} = \alpha(\mathbf{E} + \mathbf{v} \times \mathbf{B}), \quad \frac{d\mathbf{r}}{dt} = \mathbf{v}. \quad (9)$$

The electric field \mathbf{E} can be obtained from the generalized Ohm's law, which can be made dimensionless using a characteristic electric field $E_0 = v_0 B_0 / c$, and results in

$$\mathbf{E} = -\mathbf{u} \times \mathbf{B} + \frac{\epsilon}{\rho} \mathbf{J} \times \mathbf{B} - \epsilon \nabla p_e + \frac{\mathbf{J}}{R_m}. \quad (10)$$

The dimensionless parameter α relates particles and MHD field parameters:

$$\alpha = Z \frac{m_p L}{m \rho_{ii}}, \quad (11)$$

where ρ_{ii} is the proton inertial length given by $\rho_{ii} = m_p c / (e \sqrt{4\pi \rho_0})$, m is the mass of the particle, m_p is the mass of the proton, and Z is the atomic number (we will consider $m = m_p$ and $Z = 1$). The inverse $1/\alpha$ represents the nominal gyroradius, in units of L and for particles with velocity v_0 , and gives a measure of the range of scales involved in the system (from the outer scale of turbulence to the particle gyroradius). One could expect a value $\alpha > 10^4$ specially for space physics and astrophysical plasmas, which represent a huge computational challenge due to numerical limitations.

Once the turbulent state was reached, 10,000 test particles were randomly distributed in the computational box and the equation of motion for particles and the MHD electromagnetic fields were evolved. Equation (9) for each particle was evolved in time using a fourth-order Runge–Kutta method, and cubic splines were used to extrapolate the values of the terms in Equation (10) from the three-dimensional MHD grid to the position of the particles. Particles were initialized with a Gaussian velocity distribution function, with a root mean square (rms) value of the order of the Alfvén velocity. It is well known that the particle gyroradius has a significant influence on the particle acceleration mechanisms, and our aim in this paper is to explore the dynamical effect of MHD turbulence on acceleration of large gyroradius particles, of the order of the turbulent dissipation length. Thus, we set $\rho_{ii} = l_d$. We will loosely call these particles “protons” as their gyroradius is at the end of the inertial range of our MHD simulations (Dmitruk et al. 2004).

The second and third terms in Equation (10) are the Hall effect and the electron pressure gradient respectively. Those two terms can be important at small scales, starting at the proton gyroradius, but they give small contributions to the fluid equations through the curl of \mathbf{E} (i.e., single-fluid compressible MHD is still appropriate at large scales). However, one must include them in the equation of motion of the particles to have a consistent description of particles in the compressible MHD case (Kulsrud 1983), and to have consistency with kinetic descriptions of plasmas such as those in Wan et al. (2015).

The dimensionless coefficient ϵ in Equation (10) is the Hall parameter:

$$\epsilon = \frac{\rho_{ii}}{L}. \quad (12)$$

The Hall parameter relates the ion inertial length scale with the energy containing scale. Thus, for consistency with the test particle definition (see Equation (11)), we set the value of the Hall parameter $\epsilon = 1/\alpha$ in our simulations. In the MHD description it is assumed that plasma protons and electrons are in thermal equilibrium, i.e., their pressures are $p_e = p_i$. Then $p_e = p/2$ with $p = p_e + p_i$ the total pressure. For particles with $\alpha = 1/\epsilon$ and $\rho_{ii} = l_d$ (as is the case studied here), we showed in Gonzalez et al. (2016) that the second and third terms on the rhs of Equation (10) give a small contribution to the acceleration. As mentioned above, we will, however, preserve these terms for consistency. In the case of small particle

Table 1
Parameters of the Simulations Discussed in Section 3.1

Run	B_0	M	β	$\langle L \rangle$	$\langle k_d \rangle$	α
1	0	0.25	6.12	2.31	92	40
2	2	0.25	2.79	1.76	96	52.63

Note. B_0 is the amplitude of the guide field, M is the sonic mach number, β is the plasma “beta,” $\langle L \rangle$ is the average energy containing scale for the flow during the steady-state period, $\langle k_d \rangle$ is the average Kolmogorov Dissipation wavenumber, and α is the nominal particle gyroradius.

gyroradii (such as particles with the mass of electrons), which was previously reported for frozen-in-time fields in Gonzalez et al. (2016), those terms become dominant. We will leave for a future study the effect of dynamical electromagnetic fields over these kinds of particles.

3. Results

3.1. Dynamic versus Static MHD Fields

In this section, we compare the particle behavior for static and dynamic MHD fields in two different scenarios: with and without an external mean magnetic field. Table 1 presents the parameters of the flow and of the particles for the simulations in this section.

In Figure 1, we show the kinetic and magnetic energy for the time-evolving simulations with $B_0 = 0$ and $B_0 = 2$. As already mentioned, the MHD fields are initially started from a null state and a forcing is applied from the beginning of the simulation to obtain a quasi-stationary state (reached after about $\sim 12t_0$), and from that time the particles evolve simultaneously with the fields (marked as $t = 0$ in the figure). Note that the system is indeed in a turbulent steady state, with the energy fluctuating around a mean value. As a reference, once the particles are added to this flow at $t = 0$, it takes about five turnover times for the particles to cross the entire simulation box (periodic boundary conditions are used for both the fluid and the particles, and thus the most energetic particles can re-enter the box and travel larger distances).

The mean square displacement D , as a function of time is shown in Figure 2, for the simulations with $B_0 = 0$ and with $B_0 = 2$, for both the static and dynamic cases. Here (and in the velocity shown in Figure 3) particles feel a sudden displacement and acceleration at early times because they first follow a “ballistic” regime, then reach a sub-diffusive stage, which is the regime of interest for our work; the early time transient seems to be slightly different in the static and dynamic cases. Again, by “static case,” we refer to the case in which a snapshot of the fields is frozen in time and the particles are evolved using those electric and magnetic fields (as done in previous studies, see, e.g., Dmitruk et al. 2004; Dmitruk & Matthaeus 2006a; Dalena et al. 2014). In the “dynamic case” the equations of motion of the particles are evolved in time together with the MHD equations, and thus the particles are affected by the time evolution of the structures in the flow. At late times, a small difference is observed between these two cases, with a slightly larger mean displacement in the static case. Additionally, the displacement of the test particles in the z -direction in the simulation with $B_0 = 2$ changes significantly (when compared with the case with $B_0 = 0$), as a result of the test particles following the direction of the mean magnetic field. While in the

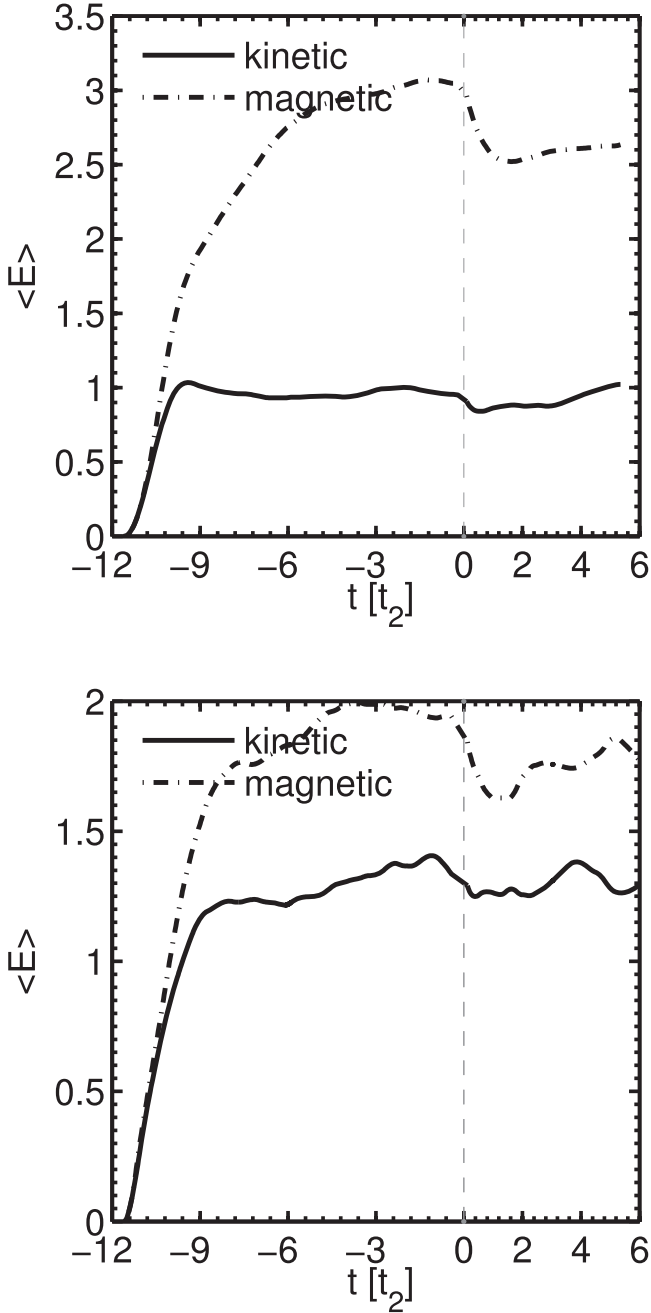


Figure 1. Mean energy of MHD variables as a function of time, (top) for a simulation with no mean magnetic field mean field simulation ($B_0 = 0$) and (bottom) for a simulation with $B_0 = 2$. The vertical dashed line denotes the particle injection time in the simulations, at the time labeled as $t = 0$.

run with $B_0 = 0$ the dispersion is isotropic (i.e., the mean displacement is the same within statistical errors for the x , y , and z directions), in the run with $B_0 = 2$ much larger displacements are observed in the z -direction.

In Figure 3, we show the mean square velocity as function of time, $v_T^2 = v_\perp^2 + v_\parallel^2$, i.e., the sum of the squared parallel and perpendicular components of the test particle velocities, averaged over all test particles. Results for the isotropic and the anisotropic cases are shown, comparing also the static and dynamic cases. A smaller mean velocity at late times is observed in the dynamic case, especially for the case with $B_0 = 2$.

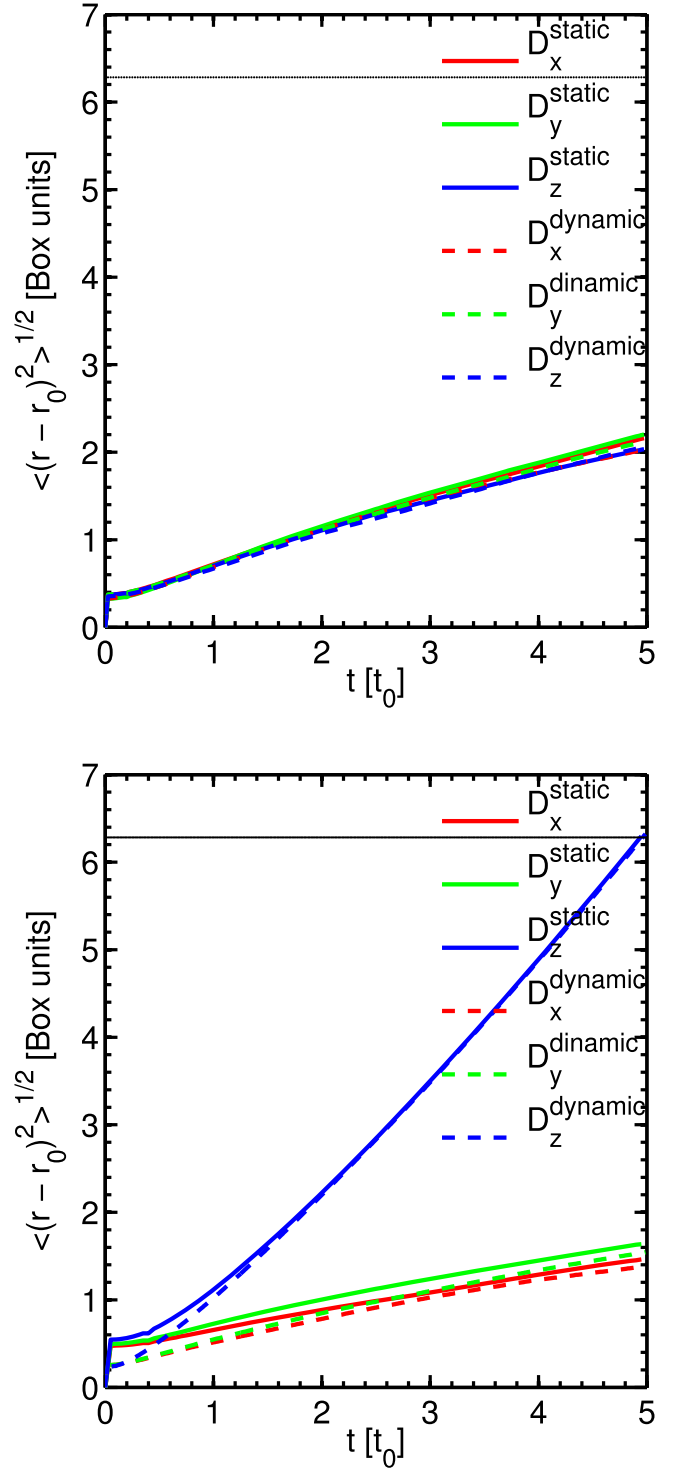


Figure 2. Mean square displacement of protons as a function of time in box units, for the static (solid line) and dynamic (dashed line) simulations. (Top) Simulation without mean magnetic field ($B_0 = 0$), and (bottom) simulation with a mean magnetic field $B_0 = 2$. The horizontal solid line indicates the size of the simulation box.

The progressive increment in the mean square velocity is largely due to the result of the interaction of the particles with the electric fields near the current sheets found along the particle trajectory, as was described in a previous paper (Gonzalez et al. 2016). In the isotropic case, the structures are randomly distributed in the box and there is no privileged

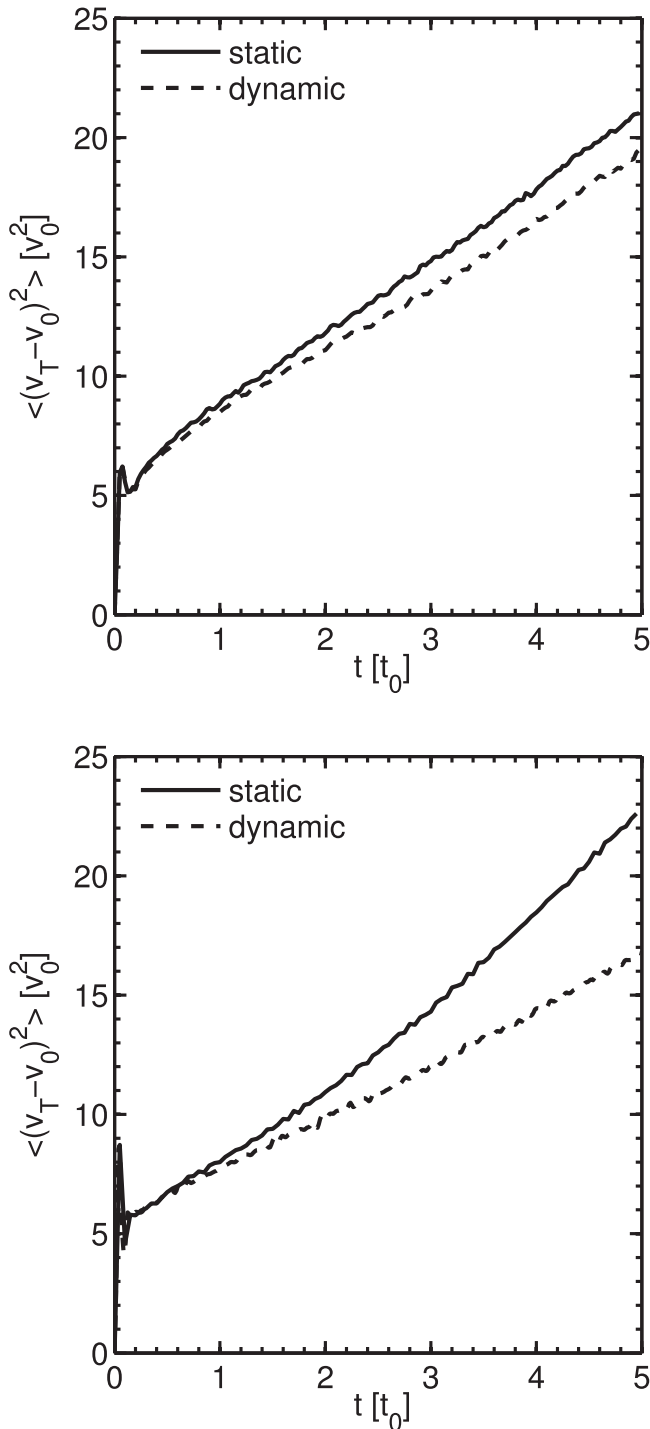


Figure 3. Mean square velocity of protons as a function of time for the static (solid line) and dynamic (dashed line) cases. (Top) Simulation without mean magnetic field ($B_0 = 0$) and (bottom) with mean magnetic field ($B_0 = 2$).

direction; as a result, the current sheets are not aligned and are instead randomly oriented. This situation and the lack of a large magnetic field make the particles interact with several different structures along its path and to be exposed regions with strong electric field gradients for long times. The smaller final rms velocity in the dynamic case is the result of the time evolution of the dynamic flow that reduces the exposure time to the strong fields, which are an essential component for efficient particle acceleration as shown below.

Figure 4 presents the time series of particle perpendicular kinetic energy and mass density along particle trajectory, for three of the most energetic particles as they move across the simulation box. Also, reversals in the current density seen by the particles are indicated by vertical dashed lines. This figure is useful to identify acceleration mechanisms in the turbulent flow. First, note the presence of fast oscillations (with the frequency of Alfvén waves at the smallest resolved scales) in the dynamic case. These oscillations are absent in the static case because the fields are frozen in time. However, particles in this case gain more perpendicular kinetic energy. Second, note an anti-correlation between density gradients and acceleration (i.e., between time derivatives of density and perpendicular kinetic energy). This behavior is caused by particles crossing compression and expansion regions that make the particles decelerate and accelerate. Thus density gradients play a role in acceleration. However, in the static case, density variations are smaller, while particle energization is significantly larger. The third important piece of information in the figure is the reversals in current density, with the vertical dashed lines indicating a particle crossing through current sheets. In the static case, frequent trapping between these structures results in energization. In the dynamic case, reversals in the current are more frequent, and current crossing and particle energization are less correlated, an indication that exposure of the particles to regions with strong electric field gradients located between current sheets is decreased.

In Figure 5, we show the probability density function (PDF) of particle energy for the isotropic and anisotropic cases (and for both the static and dynamic cases). In the isotropic case, the distributions for static and dynamic fields are very similar. Although differences in the tails have no statistical significance, there is a larger probability in the core of the distribution (i.e., for low squared velocities) in the dynamic case, which can be understood as we already noted in the dynamic case where the acceleration of particles is slightly less efficient. Moreover, in the anisotropic case, these differences become somewhat larger (although still small in absolute terms). Thus, in general, in the dynamic case, there is a larger probability of finding particles with small energy than in the static case.

To further untangle the relation between current sheet reversals and the exposure time to electric field gradients between current sheets, Figure 6 shows a scatter plot of the perpendicular particle energy versus the current density seen by particles along their trajectories for static and dynamic electromagnetic fields. To discriminate particles with low and high energy, we separate the population in four decades as indicated by the vertical dashed lines in the bottom of Figure 5 (particles with the lowest energies are in region R1, and with the highest energies in region R4).

In Figure 6, it is observed that the most energetic particles are concentrated in regions with current densities near zero, i.e., in regions where j_z changes sign. On the contrary, the current seen by particles with low energy is more dispersed. The concentration of high energy particles near $j_z \approx 0$ is more marked in the static than in the dynamic case, for which energization is also significantly larger (note the values of the squared perpendicular velocities). The scatter plot of the temporal derivative of the electric field versus the perpendicular particle energy (not shown) exhibits the same behavior, with the most energetic particles around $dE_\perp/dt \approx 0$ (where the time derivative is in respect of the time of flight of the

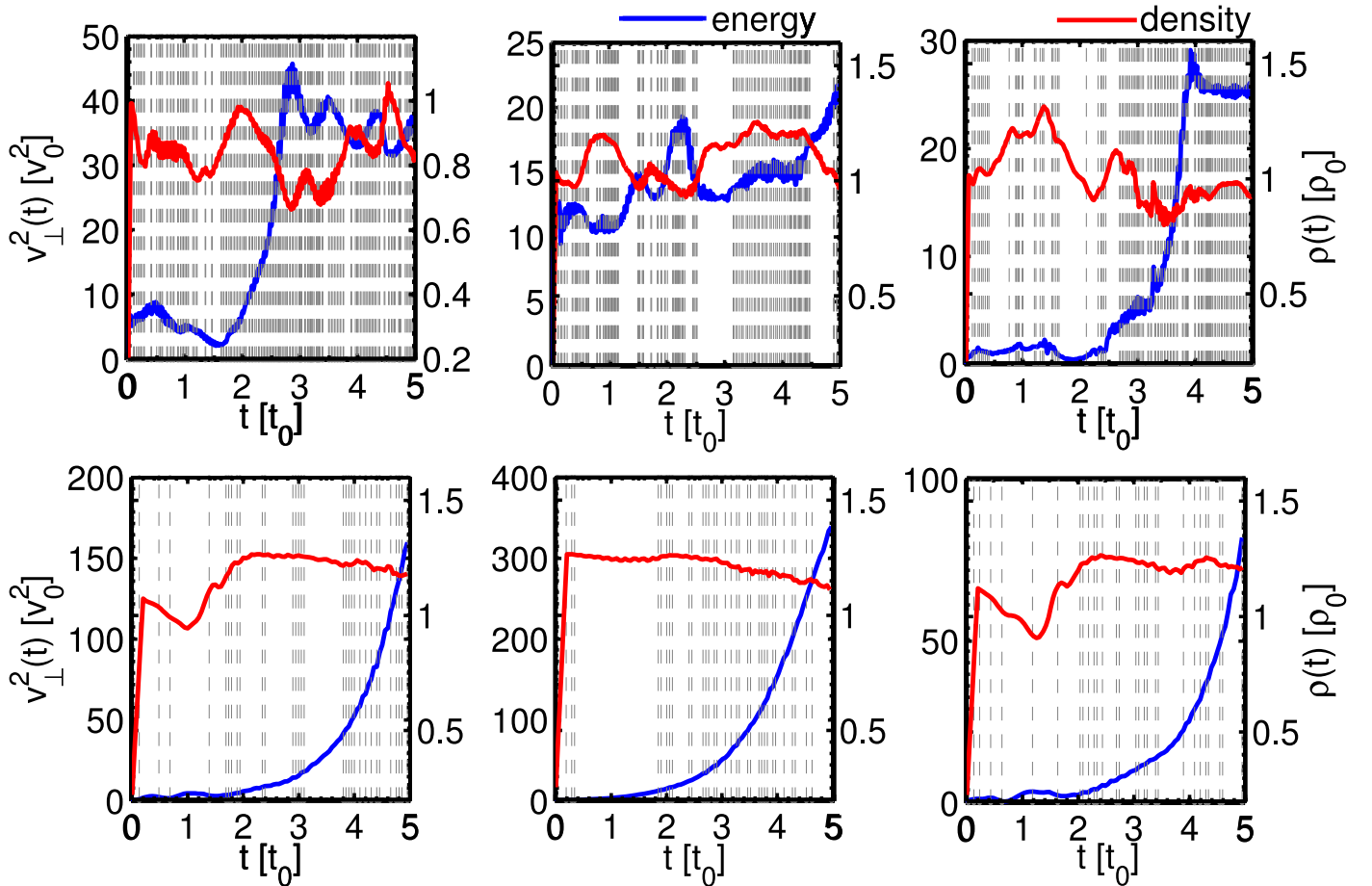


Figure 4. Particles’ perpendicular kinetic energy and local density during the flyby of three of the most energetic particles in the simulations with a mean magnetic field $B_0 = 2$: (top) simulation with dynamic fields, and (bottom) simulation with static fields. The gray vertical dashed lines show the times when the current density (j_z) seen by the particle is reversed.

particle, and is therefore proportional to the gradient observed by the particle). This confirms that particles are more accelerated when they are exposed for longer times to electric field gradients between current sheets.

As discussed above, exploration of the particles trajectories indicates that the fact that particles are more accelerated in the static case than in the dynamic case is the result of the correlation between particles and structures, and the longer exposure time with electric fields between coherent structures (i.e., particles can move from one current sheet to another, and cross strong electric field gradients in their paths with sufficient transit time to be accelerated). Meanwhile, in the dynamic case, the particles are trapped in the field lines and particles are advected by the flow. This advection reduces the particles’ exposure to the regions with strong gradients. Besides, it is important to note that there is not a single acceleration mechanism acting in a turbulent flow (as shown in Figure 4, e.g., there is a correlation also with density gradients and shock-like structures, and fast waves are also present).

With these results in mind, in the next section, we explore the effect of the mean magnetic field on particle acceleration in the dynamically evolving turbulent electromagnetic fields. To this end, we analyze particle energization varying the guide field from zero up to a strong case with $B_0 = 8$.

3.2. Effect of B_0

The aim of this section is to show the effect of the mean magnetic field B_0 on the flow features, and on the resulting particle acceleration. It is well known that MHD flows with an imposed strong magnetic field suffer a transition from a three-dimensional (3D) state toward a two-dimensional (2D) state (Alexakis 2011; Sujovolsky & Mininni 2016). The relevance of this anisotropy has been discussed by many authors in recent years, especially in the context of the solar wind problem. This transition from a 3D to a 2D state is accompanied by the transfer of energy toward modes with small parallel wavenumbers (i.e., by the increase of the correlation length of the structures in the direction of the mean field Alexakis 2011), and is associated with the development of the conditions that would establish an inverse cascade of the squared vector potential if the flow becomes 2D (Mininni et al. 2005; Wareing & Hollerbach 2010). Both effects (though in different ways) result in the growth in size of the structures in the flow. We thus now look for the effect of the resulting anisotropic field and increased correlation lengths on test particle acceleration. In Table 2, we show the parameters of the simulations presented in this section. In the table, it can be noted that the plasma beta is not equal to one, especially for the isotropic case. It is important to remark that the proton

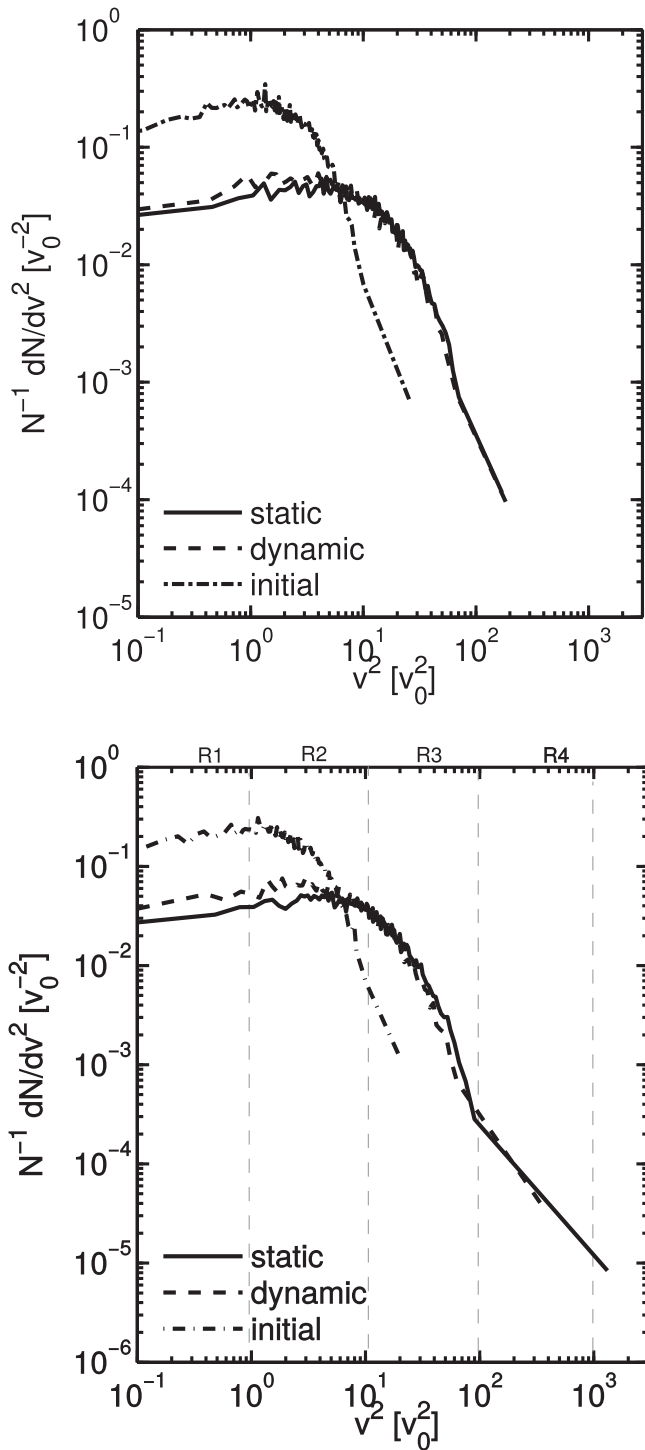


Figure 5. Probability density function of proton energies for the static and dynamic cases: (top) simulation without mean magnetic field ($B_0 = 0$) and (bottom) simulation with mean magnetic field ($B_0 = 2$).

gyroradius and the proton inertial length are not rigorously equal in those simulations.

In Figure 7, we show the rms velocity of the particles as a function of time for all the simulations with different values of the mean magnetic field. It is observed that as the mean field increases, the particle velocity at the end of the simulation is reduced, and the acceleration process is thus diminished. The reduction of the rms velocity with increasing mean magnetic field is an effect of the growth in the size of the structures; as

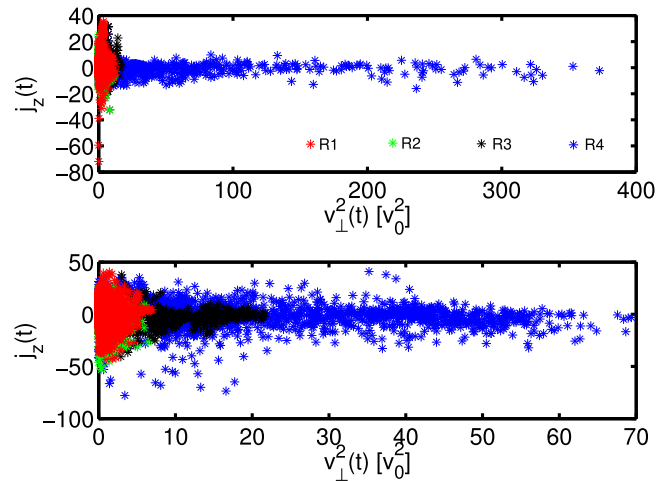


Figure 6. (Color online) Scatter plot of perpendicular particle energy vs. current density along particle trajectories. The different (color) shadings in the dots represent the energy range (from R1 to R4) of the particles in the PDF in the bottom of Figure 5: from left to right, the (color) shadings correspond to low to high energies. (Top) Simulation with static fields and (bottom) simulation with dynamic fields.

Table 2

Parameters of the Simulations with Varying B_0 , Discussed in Section 3.2

B_0	$\langle v^2 \rangle$	$\langle b^2 \rangle$	β	$\langle L \rangle$	$\langle k_d \rangle$	α
0	0.91	2.61	6.12	2.41	92	40
2	1.29	1.74	2.79	1.78	96	52.63
4	1.12	1.28	0.93	2.28	86	40
8	1.22	1.13	0.24	2.28	92.3	43.48

Note. B_0 is the amplitude of the guide field, $\langle v^2 \rangle$ and $\langle b^2 \rangle$ are, respectively, the mean kinetic and magnetic energies in the turbulent steady state (for a fluid with mass density $\rho = 1$), β is the plasma “beta,” $\langle L \rangle$ is the average energy containing scale for the flow during the turbulent steady state period, $\langle k_d \rangle$ is the average kolmogorov dissipation wavenumber, and α is the nominal particle gyroradius.

current sheets become elongated (in the direction of the mean field resulting from the anisotropy), and wider (in the direction perpendicular to the mean field resulting from the flow two-dimensionalization), the particles get trapped in the structures (i.e., the particles are magnetized) and cannot easily be exposed for longer times to the accelerating electric fields gradients in the vicinity of current sheets.

As observed before, in the isotropic case ($B_0 = 0$) particles find structures distributed in all directions, and thus the final velocity is greater than in all the other cases with non-zero mean magnetic fields. This is because the perpendicular energy gained by the the particle is decreased more substantially in the presence of a strong mean magnetic field, confirming the argument about the effect of the anisotropy mentioned above.

In Figure 8, we show the mean square magnetic moment for protons as a function of time for all the simulations with different values of the mean magnetic field. The magnetic moment $\mu = W_\perp / 2B$, with W_\perp the perpendicular energy of the particle, is one of the adiabatic invariants of charged particle dynamics in magnetic fields. Thus, it has important consequences on the dynamics of particles and determines how magnetized is a particle, that is, how much attached a particle is to a magnetic field line. Variations of the magnetic moment with turbulence parameters was studied in some detail by Dalena et al. (2012). It is observed that the mean square magnetic moment of protons increases faster in time as the

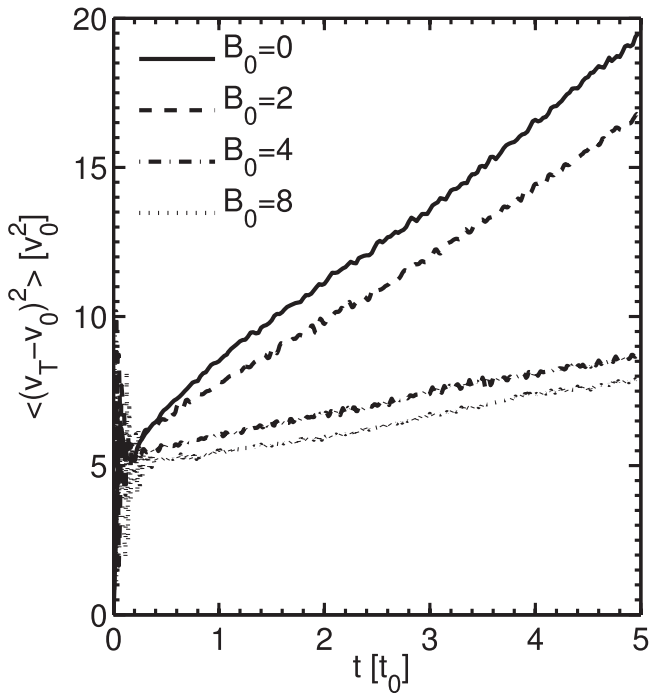


Figure 7. Mean square total velocity of protons as a function of time for different simulations, changing the mean magnetic field value B_0 .

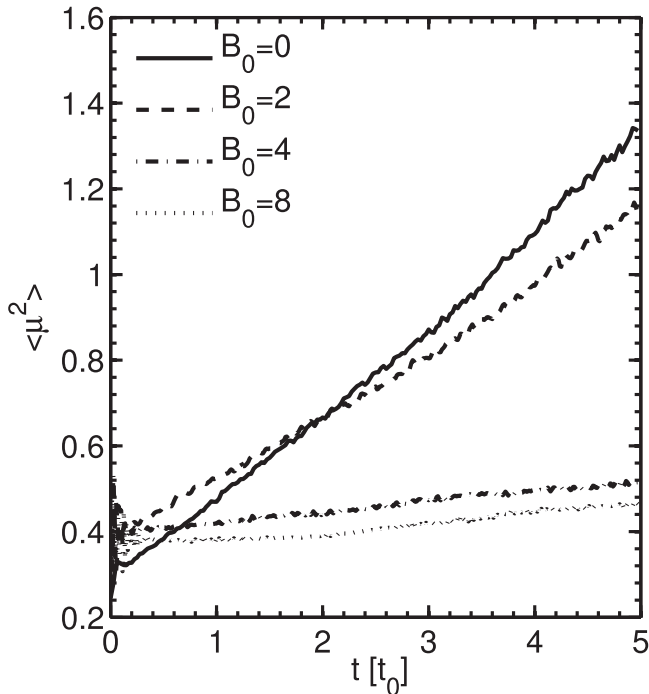


Figure 8. Mean square magnetic moment of protons as a function of time for different simulations, changing the mean magnetic field value B_0 .

mean magnetic field is decreased. This means that protons become more demagnetized for lower values of the mean magnetic field. On the other hand, as the mean magnetic field is increased, the onset of magnetic moment conservation can be observed. This means that particles become closer to being magnetized (i.e., attached to the field lines). Then, in those cases, particles propagate along the mean field direction and the perpendicular crossing through different current sheet structures becomes suppressed.

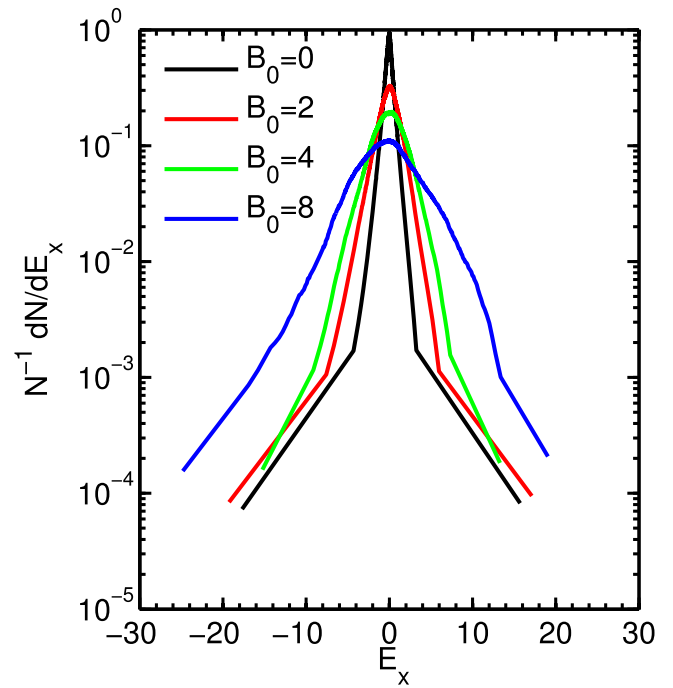
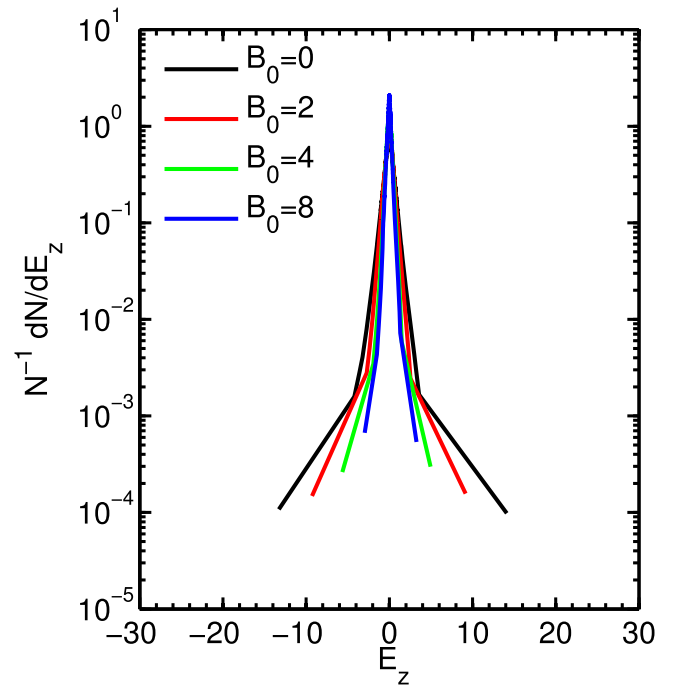


Figure 9. Probability distribution function of the electric field in all simulations. (Top) The parallel (z -component) of the electric field E_z , and (bottom) the perpendicular (x -component) of the electric field E_x .

The PDFs of the values of the electric field Cartesian components also help us to understand this scenario. They are shown in Figure 9. The parallel (z -component) of the electric field takes larger values in the isotropic case than in the anisotropic cases. As already mentioned, this is because current sheets in the former case are oriented in all directions. As B_0 is increased, the parallel (z -component) of the electric field becomes weaker. The perpendicular (x -component) of the electric field shows the opposite behavior: electric field values are larger as the mean magnetic field increases. This is caused mainly by the first term in Equation (10) (the term containing

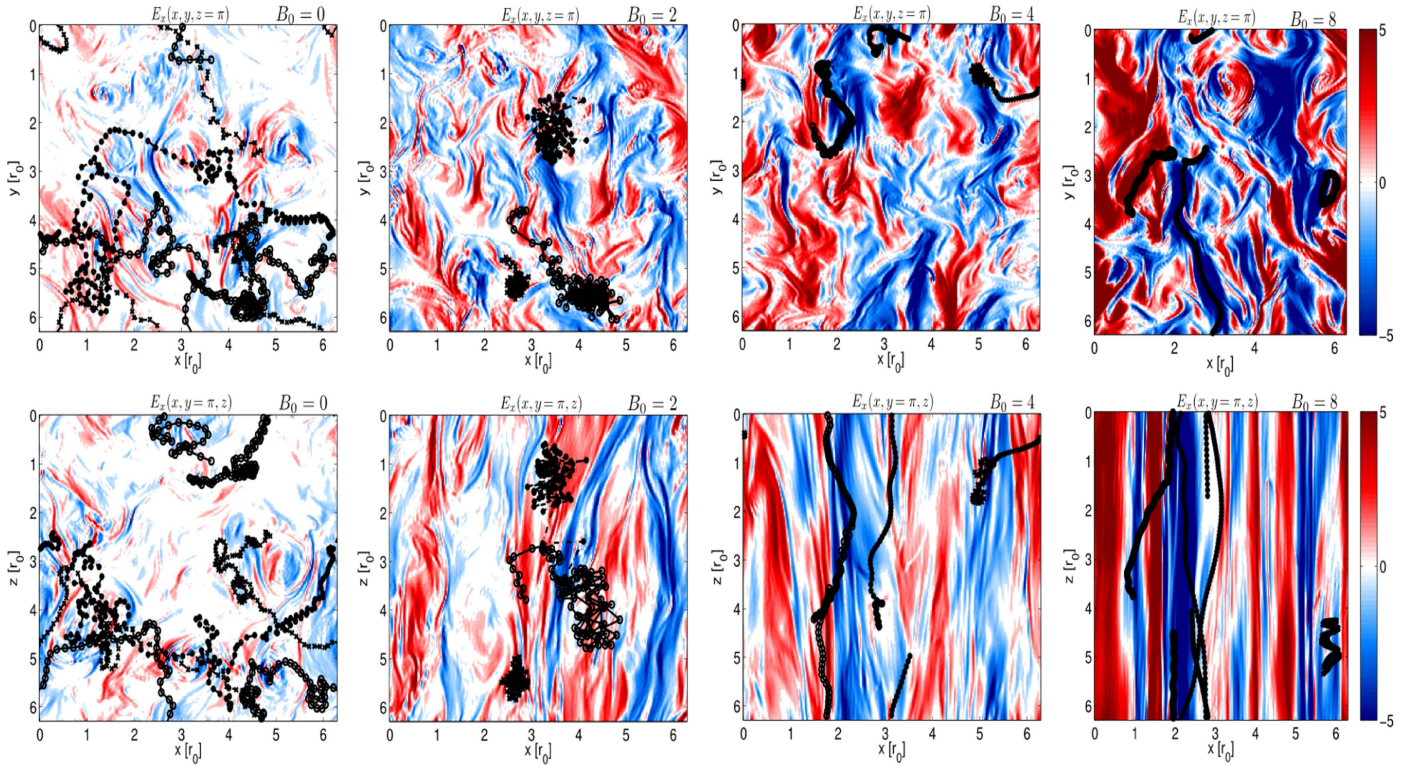


Figure 10. (Top row) x - y cross-section of the perpendicular (x -component) electric field (E_x) in the simulation box, for different values of B_0 . (Bottom row) x - z cross-section of the perpendicular (x -component) electric field (E_x). In both rows, from left to right, the following simulations are shown: $B_0 = 0$, $B_0 = 2$, $B_0 = 4$, and $B_0 = 8$ respectively. The black signs and lines show the trajectories of three of the most energetic protons in each simulation.

the mean magnetic field value). In spite of this, particle energization does not follow the same tendency because, as is noticed, the particles cannot leave the current’s structures and then cannot interact with strong electric field gradients in regions nearby the current sheet interfaces. That is, what is relevant for perpendicular particle energization is not the absolute value of the electric field but rather the exposure time of particles to strong gradients of that electric field.

To confirm this scenario, in Figure 10, we show the x - y cross-section of the perpendicular component of the electric field E_x , and the x - z cross-section of E_x for all the simulations discussed in this section (from left to right, we show the cases with $B_0 = 0$ up to the strongest case with $B_0 = 8$). The trajectory of three of the most energetic particles are shown as well with solid lines and marks (using pluses, circles, and crosses for each particle).

Note the particle behavior and the importance of the structure size on particle energization. In the isotropic case, it is observed that the structures are distributed in all directions, and there are no differences between both cross-sections of the electric field. In contrast, the cases with non-zero mean magnetic fields show the structures aligned with the mean field as clearly seen in the bottom panels of Figure 10. As the mean magnetic field increases, the flow becomes more anisotropic and for the strongest mean field the variations in the z -direction are small.

The x - y cross-sections also give us an idea of the size of the structures. It is observed that as the mean magnetic field increases, the width of the structures also increases, and a transition from a flow with randomly distributed structures with a width of the order of the dissipation scale can be seen for the

isotropic case, moving toward a flow with wider structures in the cases with a non-zero mean magnetic field.

The trajectories of the particles show the importance of the structure size. While trajectories reminiscent of stochastic motion are observed at the isotropic case, where the particle passes through many structures finding strong electric field gradient regions along its path, as the mean magnetic field increases, the particle trajectories become more elongated and particles cannot go across structures. For the $B_0 = 4$ and $B_0 = 8$ cases, the trajectories show that particles drift across a few structures, almost staying around a single one and no longer allowing the particle to stay in strong electric field gradient regions. This is the reason why particles do not gain as much energy as in the isotropic case, as the random hopping from one structure to the next is, at least in the static case, the most efficient acceleration mechanism as observed in Gonzalez et al. (2016).

4. Discussion

In this paper, we studied the effect of dynamically evolving MHD turbulence on test particle acceleration. To this end, we numerically solved the MHD equations, and solved the equations for test particles either together with the flow evolution, or in frozen-in-time fields obtained from snapshots of the electromagnetic fields in the MHD simulations. This case of “static MHD turbulence” has been used before to investigate particle energization phenomena (Dmitruk et al. 2004; Dalena et al. 2014; Gonzalez et al. 2016). We found some differences between both models, with a slight reduction of particle acceleration in the dynamical case. This result was obtained for “protons,” or test particles with gyroradii of the order of the

flow dissipation scale, which is the case we specifically analyzed here. The cause for the small reduction in the acceleration rate is particle trapping in dynamic field lines, which makes it more difficult for particles to stay long enough in regions of strong electric field gradients located at the interface between structures whereby particles are accelerated.

The study was motivated by the fact that several of the previous works done on particle acceleration considered static MHD turbulence. Even though there are some previous papers that have dealt with the dynamic problem (Cho & Lazarian 2006; Teaca et al. 2014; Weidl et al. 2015; Hussein & Shalchi 2016), most of those studies consider incompressible flow models. Also, a detailed comparison between static and dynamic fields and their effect of particle acceleration was lacking.

This paper is most closely related with Lehe et al. (2009) due to the compressible turbulence and dynamic model that both used. In that paper, the authors conclude that the particle heating is due to the cyclotron resonance with Alfvén waves in the system when the wave frequencies are of the order of the particle gyrofrequency. In this paper, we have shown that perpendicular proton heating is very similar for the dynamic and static cases, which means that we can obtain the same results with or without waves in the system. This is very important because it confirms the importance of coherent structures in particle energization. The authors also discussed the relevance of the results in the context of solar wind and solar corona, and they claim that the results cannot be directly applied to those astrophysical systems, mainly because of the limitation in numerical resolution and scale separation one can obtain using numerical methods. We agree with the authors about the need to extrapolate these results to a higher numerical resolution, which could result in an asymptotic study that is more closely related to the corona and the solar wind.

Additionally, we investigated the effect of anisotropy caused by the mean magnetic field on the resulting particle acceleration, for which an adverse effect on particle energization was observed. The transition from a three-dimensional to a two-dimensional MHD state, which can also be accompanied by an inverse energy cascade for very strong magnetic guide fields, causes an increase in the structure sizes, impacting the reduction of the particle acceleration because test particles are trapped in wider current channels and exhibit an almost magnetized state with conservation of magnetic moment.

Considering the results reported in Gonzalez et al. (2016), where we showed that the flow compressibility affects particle energization, in this work, we made sure that no important variations on the turbulent Mach number were present between different runs. To this end, we also considered forced simulations (instead of freely decaying ones), to be able to study particle acceleration in a turbulent steady state with a well defined mean Mach number. To prevent effects associated with a possible inverse cascade of magnetic helicity, or of cross-correlations between the velocity and magnetic fields, we implemented a forcing mechanism that guarantees no net injection of kinetic helicity, magnetic helicity, or cross-helicity.

In the same way, the model we use in this paper for the test particles includes electron pressure effects and the Hall current in the generalized Ohm's law for particle motion computation. It is noted that we have not included those terms in the induction equation, based on the assumption that we can neglect them at large fluid scales (Dmitruk & Matthaeus 2006a, 2006b). While,

in a previous study, we found that retaining those effects can have an important contribution to the energization of particles with small gyroradius (Gonzalez et al. 2016; compared with the width of the current sheets), for particles with gyroradius of the order of the MHD dissipation scale (called "protons" here), these effects are not as important. However, these terms (albeit they give a small contribution), and other acceleration mechanisms, coexist in the turbulent flow with the observed acceleration as particles jump from one current sheet to another. This is the case of the particle interaction with compression regions (as, e.g., shock structures), which also results in particle acceleration. We have shown a correlation between changes in density and changes in particle energy, which seem to be more important in the dynamic case.

While we have found a difference in effectiveness of different mechanisms in energizing small gyroradius particles (electrons) and larger gyroradius particles (protons), as in Dmitruk et al. (2004), it is worthwhile to recall that in the test particle simulations of Dalena et al. (2014) were carried out for a long enough time to observe the transition between these two regimes for a single particle species. This requires following the most energetic particles for thousands of gyroperiods. The reported mechanism for the second-stage higher rigidity energization in that (static) numerical experiment is completely compatible with what we found here and described above. In an initial epoch, low rigidity acceleration is due to trapping in magnetic structures and is predominantly parallel acceleration. In this regime, numerous theoretical treatments mentioned in the introduction are relevant (Matthaeus et al. 1984b; Dmitruk et al. 2004; Drake et al. 2005, 2006; Oka et al. 2010; Dahlin et al. 2014; Guo et al. 2014; Li et al. 2015) and have provided physical insight concerning the several processes that contribute to this energization. For the larger gyroradius case, to which the present study is relevant, different analyses become relevant (Dmitruk et al. 2004; Chandran et al. 2010). In particular, in the present results, relevant to suprathermal protons, changes in the magnetic moment become important, and the perpendicular electric field plays a central role, both of which stand in contrast to the low rigidity electron case.

It is important to mention that there are also more complete frameworks (e.g., Zank et al. 2014; le Roux et al. 2015) that include at least several of the dynamical mechanisms that are relevant here, such as interactions with secondary islands and anti-reconnection electric fields, and magnetic flux rearrangements (and associated electric fields) due to island contraction and merging. These theoretical frameworks are quite flexible and can accommodate a wide range of modeled physical effects, including pitch angle scattering.

In order to make connections with those above referenced works, which are based on transport formalism, it is noted that here we have studied the dynamics of particles having gyroradii comparable to the boundary layer regions near the edge of flux tube, likely near reconnection sites. Such particles are not readily trapped within the current sheets or the smaller numerous secondary islands that form nearby, because these structures have scales of the order of the ion inertial scale or the thermal proton gyroradius. Such particles encounter steep perpendicular electric field gradients, magnetic compressions, and multiple current sheets, which are associated with flux tube interactions (and flux pileup). This type of process, as studied here, is also fairly local, as seen in Figure 10, and therefore does not require a transport equation approach that describes

many such interactions. Eventually, it would be very useful to have a transport formulation to treat the multiple-encounter version of the case that we study, analogous to the framework described in Zank et al. (2014) and le Roux et al. (2015), but that would clearly lie well beyond the scope of our study.

In general, the results support and reaffirm the importance of coherent structures on particle acceleration and their possible relevance for the solar wind. This latter problem has been analyzed using different approaches, from spacecraft data measurements (Tessein et al. 2015) to different numerical schemes covering fluid and kinetic descriptions (Ambrosiano et al. 1988; Drake et al. 2006; Greco et al. 2008; Karimabadi et al. 2013; Servidio et al. 2014; Wan et al. 2015). The coherent structures in these cases appear by the interaction and pileup of magnetic flux tubes, and those regions provide the possibility of generating strong field gradients, where particles can experience substantial energization. Also, numerical simulations with a complete kinetic description (Wan et al. 2015) have shown a correlation between regions of energy dissipation and regions near strong current density enhancements (of the order of particle scales, especially at the ion inertial length). The extended model used for the particles, including Hall and electron pressure effects, allow for better comparison with these kind of models. This is left for future work, through direct comparison between kinetic, hybrid simulations, and test particles.

C.A.G., P.D.M., and P.D. acknowledge support from grants UBACyT No. 20020110200359 and 20020100100315, and from grants PICT No. 2011-1529 and 2011-0454. W.H.M. was partially supported by NASA LWS-TRT grant NNX15AB88G, Grand Challenge Research grant NNX14AI63G, and the Solar Probe Plus mission through the Southwest Research Institute ISIS project D99031L.

ORCID iDs

W. H. Matthaeus  <https://orcid.org/0000-0001-7224-6024>

References

- Alexakis, A. 2011, *PhRvE*, **84**, 056330
 Ambrosiano, J., Matthaeus, W. H., Goldstein, M. L., & Plante, D. 1988, *JGRA*, **93**, 14383
 Bieber, J. W., Matthaeus, W. H., Smith, C. W., et al. 1994, *ApJ*, **420**, 294
 Chandran, B. D. G. 2003, *ApJ*, **599**, 1426
 Chandran, B. D. G., Li, B., Rogers, B. N., Quataert, E., & Germaschewski, K. 2010, *ApJ*, **720**, 503
 Chandran, B. D. G., & Maron, J. L. 2004, *ApJ*, **603**, 23
 Chen, C. H. K., Leung, L., Boldyrev, S., Maruca, B. A., & Bale, S. D. 2014, *GeoRL*, **41**, 8081
 Cho, J., & Lazarian, A. 2006, *ApJ*, **638**, 811
 Dahlin, J. T., Drake, J. F., & Swisdak, M. 2014, *PhPI*, **21**, 092304
 Dalena, S., Greco, A., Rappazzo, A. F., Mace, R. L., & Matthaeus, W. H. 2012, *PhRvE*, **86**, 016402
 Dalena, S., Rappazzo, A. F., Dmitruk, P., Greco, A., & Matthaeus, W. H. 2014, *ApJ*, **783**, 143
 Dmitruk, P., & Matthaeus, W. H. 2006a, *JGRA*, **111**, A12110
 Dmitruk, P., & Matthaeus, W. H. 2006b, *PhPI*, **13**, 042307
 Dmitruk, P., Matthaeus, W. H., & Seenu, N. 2004, *ApJ*, **617**, 667
 Drake, J. F., Shay, M. A., Thongthai, W., & Swisdak, M. 2005, *PhRvL*, **94**, 095001
 Drake, J. F., Swisdak, M., Che, H., & Shay, M. A. 2006, *Natur*, **443**, 553
 Gonzalez, C. A., Dmitruk, P., Mininni, P. D., & Matthaeus, W. H. 2016, *PhPI*, **23**, 082305
 Greco, A., Chuychai, P., Matthaeus, W. H., Servidio, S., & Dmitruk, P. 2008, *GeoRL*, **35**, L19111
 Guo, F., Li, H., Daughton, W., & Liu, Y.-H. 2014, *PhRvL*, **113**, 155005
 Hussein, M., & Shalchi, A. 2016, *ApJ*, **817**, 136
 Jokipii, J. R. 1966, *ApJ*, **146**, 480
 Karimabadi, H., Roytershteyn, V., Wan, M., et al. 2013, *PhPI*, **20**, 012303
 Khabarova, O. V., Zank, G. P., Li, G., et al. 2016, *ApJ*, **827**, 122
 Kulsrud, R. M. 1983, *Basic Plasma Physics*, ed. A. A. Galeev & R. N. Sudan, (Amsterdam: North-Holland Publishing Company)
 Lazarian, A., Vlahos, L., Kowal, G., et al. 2012, *SSRv*, **173**, 557
 le Roux, J. A., Zank, G. P., Webb, G. M., & Khabarova, O. 2015, *ApJ*, **801**, 112
 Leamon, R. J., AaaSmith, C. W., Ness, N. F., Matthaeus, W. H., & Wong, H. K. 1998, *JGR*, **103**, 4775
 Lehe, R., Parrish, I. J., & Quataert, E. 2009, *ApJ*, **707**, 404
 Li, X., Guo, F., Li, H., & Li, G. 2015, *ApJL*, **811**, L24
 Lynn, J. W., Quataert, E., Chandran, B. D. G., & Parrish, I. J. 2013, *ApJ*, **777**, 128
 Matthaeus, W. H., Ambrosiano, J. J., & Goldstein, M. L. 1984a, *PhRvL*, **53**, 1449
 Matthaeus, W. H., Ambrosiano, J. J., & Goldstein, M. L. 1984b, *PhRvL*, **53**, 1449
 McComas, D. J., Velli, M., Lewis, W. S., et al. 2007, *RvGeo*, **45**, RG1004
 Mininni, P. D. 2011, *AnRFM*, **43**, 377
 Mininni, P. D., Montgomery, D. C., & Pouquet, A. G. 2005, *PhFI (1994-present)*, **17**, 035112
 Mininni, P. D., Rosenberg, D., Reddy, R., & Pouquet, A. 2011, *ParC*, **37**, 316
 Oka, M., Phan, T.-D., Krucker, S., Fujimoto, M., & Shinohara, I. 2010, *ApJ*, **714**, 915
 Parker, E. N., & Tidman, D. A. 1958, *PhRv*, **111**, 1206
 Pouquet, A., & Patterson, G. S. 1978, *JFM*, **85**, 305
 Servidio, S., Osman, K. T., Valentini, F., et al. 2014, *ApJL*, **781**, L27
 Subedi, P., Sonsrrette, W., & Blasi, P. 2017, *ApJ*, **837**, 140
 Sujovolsky, N. E., & Mininni, P. D. 2016, *PhRvF*, **1**, 054407
 Teaca, B., Weidl, M. S., Jenko, F., & Schlickeiser, R. 2014, *PhRvE*, **90**, 021101
 Tessein, J. A., Ruffolo, D., Matthaeus, W. H., et al. 2015, *ApJ*, **812**, 68
 Wan, M., Matthaeus, W. H., Roytershteyn, V., et al. 2015, *PhRvL*, **114**, 175002
 Wareing, C. J., & Hollerbach, R. 2010, *JPIPh*, **76**, 117
 Weidl, M. S., Jenko, F., Teaca, B., & Schlickeiser, R. 2015, *ApJ*, **811**, 8
 Zank, G. P., le Roux, J. A., Webb, G. M., Dosch, A., & Khabarova, O. 2014, *ApJ*, **797**, 28